Deep–Sea Research I 162 (2020) 103307

Contents lists available at ScienceDirect

Deep-Sea Research Part I

journal homepage: http://www.elsevier.com/locate/dsri

The characteristics of the mid-depth striations in the North Indian Ocean

Yifan Xia [a,b], Yan Du [a,b,c,*], Bo Qiu [d], Xuhua Cheng [e], Tianyu Wang [a], Qiang Xie [f]

[a] State Key Laboratory of Tropical Oceanography, South China Sea Institute of Oceanology (SCSIO) and China-Pakistan Joint Research Center on Earth Sciences, Chinese Academy of Sciences (CAS), Guangzhou, China
[b] University of Chinese Academy of Sciences, Beijing, China
[c] Southern Marine Science and Engineering Guangdong Laboratory, Guangzhou, China
[d] Department of Oceanography, University of Hawaii at Mānoa, Honolulu, HI, USA
[e] College of Oceanography, Hohai University, Nanjing, China
[f] Institute of Deep-Sea Science and Engineering, CAS, Sanya, China

ARTICLE INFO

Keywords:
Baroclinic rossby wave
Striations
Triad rossby wave interaction

ABSTRACT

Argo float trajectory data has been used to estimate the velocities of mid-depth (1000 db) currents in the North Indian Ocean (NIO). The structure of the upper ocean absolute geostrophic currents can be derived more accurately from the Argo temperature and salinity profiles by referring to the estimated velocities rather than by assuming a level of "no motion". The derived flow field reveals that the eastward zonal velocities generate striation-like structures in the Arabian Sea, which is most prominent above the layer of 500 db layer, with a meridional scale of ~300 km; however, such structures are barely observed in the Bay of Bengal. This meridional scale as well as the distribution of the mid-depth striations are unique to the NIO, as compared with the other ocean basins. The nonlinear $1\frac{1}{2}$-layer reduced-gravity model combined with the triad baroclinic Rossby wave interaction theory have been used to determine the essential factors controlling the characteristics of the quasi-zonal striation structure. Compared with the North Pacific Ocean, the meridional scale in the NIO is narrower, and is caused by the smaller basin size in the equatorial zone, rather than by the semiannual wind stress forcing period or the eastern boundary angle. Furthermore, the coastal trapped Kelvin waves significantly contribute to the generation of the zonal striations in the Arabian Sea.

1. Introduction

Alternating zonal flows are universally pervasive in the atmosphere and oceans of giant rotating planets. For instance, such alternating zonal flows formed by the clouds on Jupiter are noticeable in the snapshots taken by astronomical telescopes (Galperin et al., 2004). In the oceans of the Earth, the magnitude of the zonal jet velocities is lower than or comparable to those of the mesoscale eddies in the subtropics (Berloff et al., 2009a; Galperin and Read, 2019); these oceanic quasi-zonal jets are often referred to as striations (e.g., Wang et al., 2012, and references therein). Typically, the averaged velocities are not only about a few centimeters per second with meridional scales of ~200−600 km (Maximenko et al., 2005), but also more distinct below the main thermocline, which is unaffected by the surface wind-driven circulation.

Several previous works indicate the existence of mid-depth striations in the tropical regions of the Pacific and Atlantic oceans (Cravatte et al., 2012, 2017; Qiu et al., 2013a, b; van Sebille et al., 2011). Furthermore, similar zonal striation structures were independently observed, based on the Argo float trajectories (Cravatte et al., 2012; Ascani et al., 2010, 2015; Belmadani et al., 2013) or T/S profiles (Qiu et al., 2013a, b). Cravatte et al. (2017) further combined these two types of data to demonstrate geostrophic velocity reconstruction by considering the 1000 db velocity derived by the Argo float trajectory data as a reference layer, rather than by assuming a "no motion" layer at 2000 db.

Furthermore, recent studies have explored dynamic mechanisms of the striation-like structures. One commonly adopted theory is the arrest of the inverse energy cascade by barotropic Rossby waves in a two-dimensional turbulent ocean (Rhines, 1975); the meridional scale is regarded as the Rhines arrest scale (Rhines, 1975; Nakano and Hasumi, 2005; Galperin et al., 2004; Richards et al., 2006). However, some researchers reported that this scale is inconsistent with the observations (Maximenko et al., 2005; Berloff et al., 2009a), and also suggested that

* Corresponding author. State Key Laboratory of Tropical Oceanography, South China Sea Institute of Oceanology (SCSIO), Chinese Academy of Sciences (CAS), Guangzhou, China.
E-mail address: duyan@scsio.ac.cn (Y. Du).

https://doi.org/10.1016/j.dsr.2020.103307
Received 28 November 2019; Received in revised form 2 May 2020; Accepted 2 May 2020
Available online 12 June 2020

most of the cascading energy can overcome the "arrest" (Berloff et al., 2009b). Furthermore, Wang et al. (2012) demonstrated the effect of unstable eastern boundary currents using a simple quasi-geostrophic model, while Qiu et al. (2013b) used a nonlinear $1\frac{1}{2}$-layer reduced-gravity model to demonstrate that the Pacific North Equatorial Undercurrent (NEUC) jets are generated by the wind-forced annual baroclinic Rossby wave interactions. Moreover, Berloff (2005) proved similar dynamics that the generation of the zonal jets is a result of the nonlinear interactions of resonant basin modes.

However, there have been relatively few studies focusing on the mid-depth quasi-zonal jets or the striation-like structures in the North Indian Ocean (NIO). Unlike the other oceans, the NIO is characterized by a seasonal monsoon system (Schott et al., 2009); the semiannual zonal wind is dominant on the equatorial Indian Ocean (Ogata and Xie, 2011), while the monsoon-driven circulations are complicated. Davis (2005) attempted to examine the mid-depth circulation in the Indian Ocean using hundreds of autonomous floats, and reported that the striation-like structure of the currents is indistinct, especially in the Bay of Bengal; this is probably because of the insufficient float data. Ollitrault and de Verdiere (2014) used the Argo float trajectory data to estimate the global mid-depth current. They observed the existence of alternating zonal bands among three oceans; however, these jets were not well defined in the Indian Ocean. Fig. 1 shows 13 Argo floats trajectories at their parking depth of 1000 db, wherein the surface drifting errors have been removed, and the vertical shear errors are relatively small. Thus, their movements can be regarded as the background velocities at their respective parking depths. The results suggest that the possible existence of alternating quasi-zonal flows at 1000 db in the Arabian Sea. The objective of our study is to determine the realistic mid-depth currents in the NIO and explore the underlying dynamics.

This paper is organized as follows: In Section 2, we describe the data and method and construct the geostrophic quasi-zonal velocity data for each layer ranging from the surface to 1200 db. Section 3 demonstrates the characteristics of the mid-depth currents based on the Argo float trajectory data. Referring to the float-derived 1000 db layer velocity, we examine the quasi-zonal currents in the NIO and compare them with the modeled currents based on the eddy-resolving OFES model output. In Section 4, we use a nonlinear $1\frac{1}{2}$-layer reduced-gravity model combined with the triad Rossby wave interaction theory to explain and discuss the model results, which indicate that the meridional scale of the observed striations in the NIO is smaller than that in the North Pacific Ocean, and unravel the generation mechanism of the striations. Finally, Section 5 presents the summary of the study.

2. Data

2.1. Argo float data and mapping method

Within the NIO domain (45°-100°E, 0°-30°N), over 46,000 Argo profiles were acquired between January 2004 and December 2016. The trajectories of these floats were analyzed to obtain the time-mean jets under the thermocline. Fig. 2 shows the distributions of the floats as a function of space and time, with reasonable data coverage. We obtained 11,312 profiles in MAM, 11,784 in JJA, 11,865 in SON, and 11,574 in DJF. These profiles in different seasons are equivalent in number, and no bias was involved in the seasonal sampling of the float data. The mean Argo temperature and salinity gridded climatology at 1/6° resolution was obtained from Roemmich et al., 2009 and updated to include 2004–2016. The vertical resolution of this climatology is 10m down to 180m, 20m between 180 and 500m, 50m between 500 and 1400m, and 100m between 1400 and 2000m.

With the advancement in estimation and quality control, Argo float trajectory data products, such as YoMaHa'07 and ANDRO, have become essential in the study of deep ocean circulation (Lebedev et al., 2007; Ollitrault and Rannou, 2013). According to YoMaHa'07 data, striation-like jets were observed in the North Pacific as well as in the global ocean (Ascani et al., 2010, 2015; Belmadani et al., 2013). However, YoMaHa'07 failed to capture the clear structure of the NIO striations (Ascani et al., 2010); and moreover, to our knowledge, the ANDRO dataset is not available for public for some data centers since 2010 January. Therefore, we constructed a new dataset for the present study by the following process: we acquired the trajectory data from January 2004 to December 2016 by adopting a strict quality control, and then used extrapolation to eliminate the surface drifting errors (Park et al.,

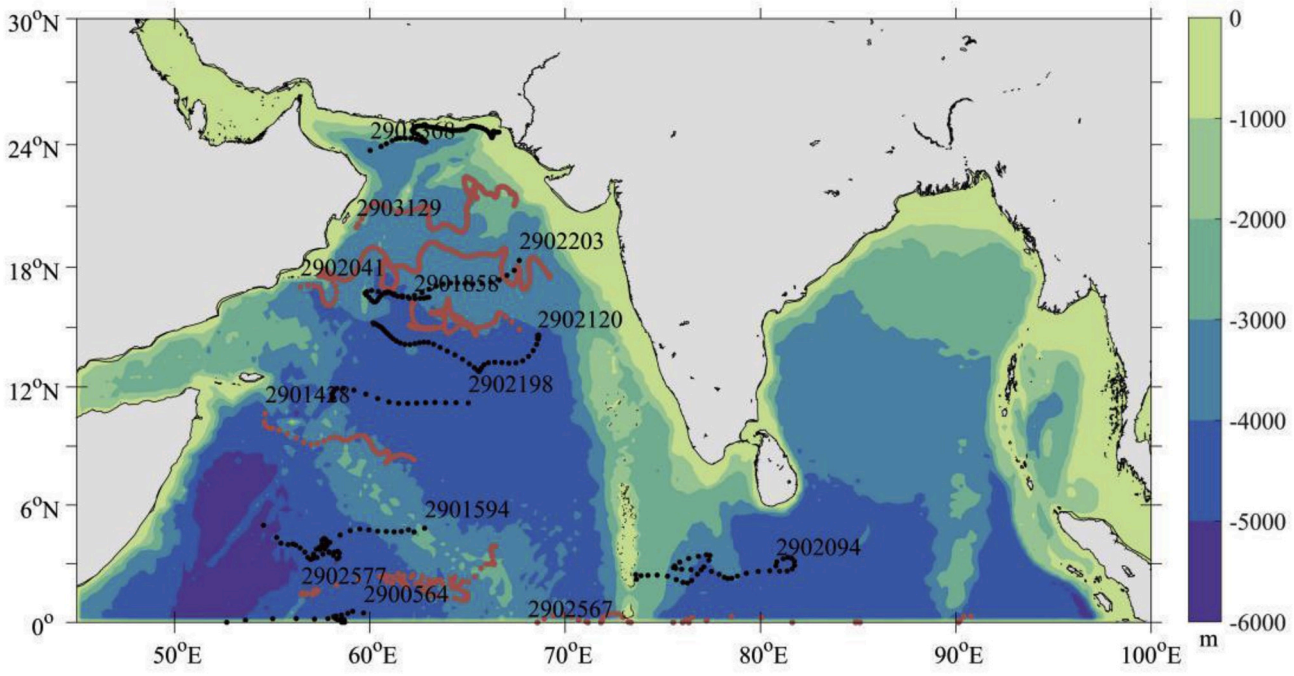

Fig. 1. Bottom topography of the North Indian Ocean (NIO) (shaded), and 13 Argo floats at 1000 db which have zonal trajectories (under a five-point moving average). The red/black dots indicate the eastward/westward moving floats. The surface drifting errors have been removed (Park et al., 2005).

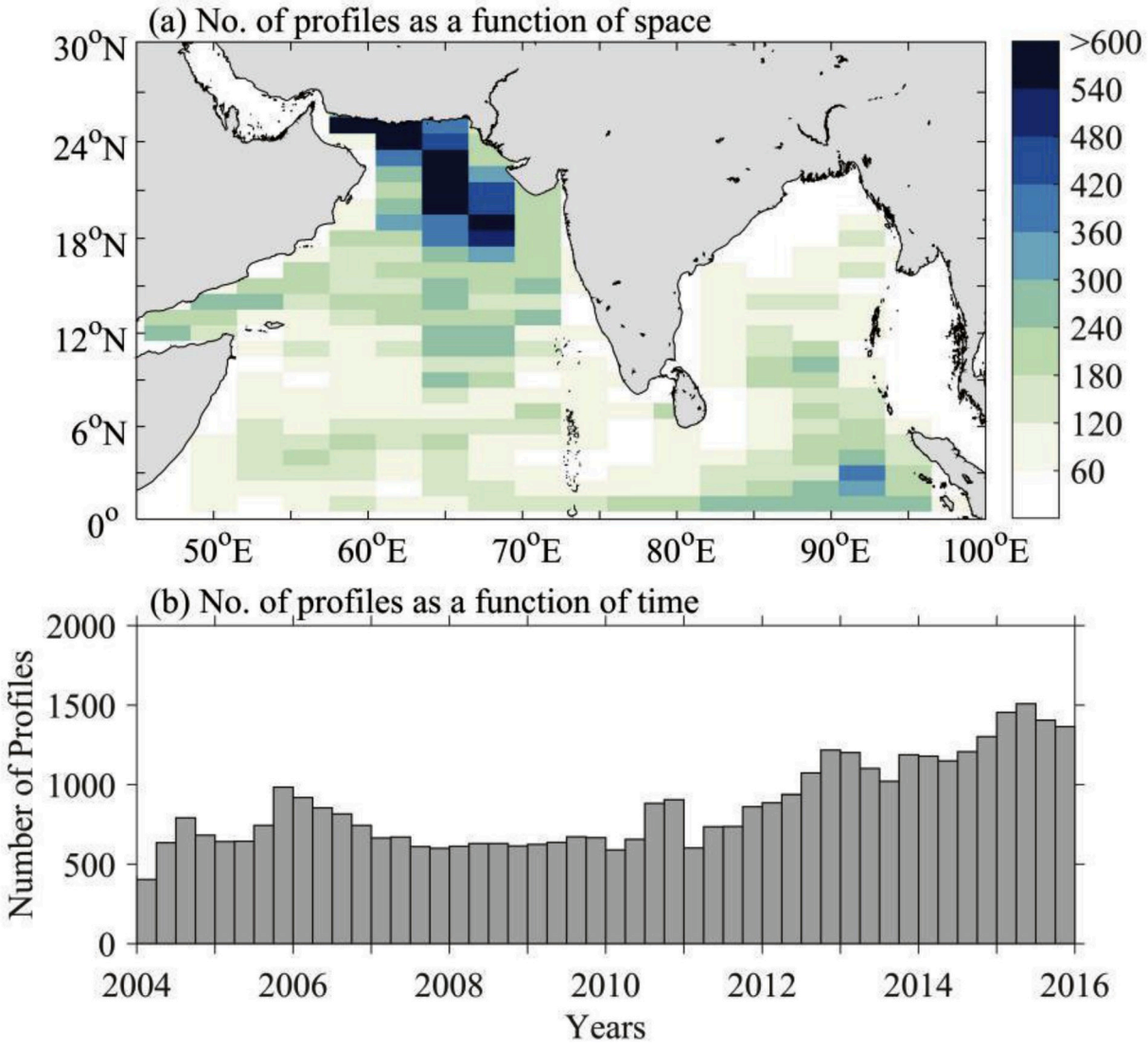

Fig. 2. Distribution of the Argo profiles in the NIO between January 2004 and December 2016. (a)Number of profiles in the 3° longitude and 1° latitude boxes. (b) Histogram of the profile numbers (bin width is 3 months).

2004, 2005; Park and Kim, 2013; Xie and Zhu, 2008; Ollitrault and Rannou, 2013). For the period prior to January 2010, we compared our new dataset with that of the ANDRO in Fig. 3 and found consistence between the striation locations. The trajectory data were then mapped onto a 0.5° latitude and 2° longitude grid by the objective mapping technique using the Gaussian weight function: $\exp[-(\Delta x^2)/(2L_x^2) - (\Delta y^2)/(2L_y^2)]$, where Δx and Δy are the zonal and meridional distances between a data point and the grid point respectively. Qiu et al. (2013a) used $L_x = 2°$ and $L_y = 0.5°$ for the North Pacific, and Cravatte et al. (2012) used $L_x = 3°$ and $L_y = 0.5°$ for the tropical Pacific. Herein we selected $L_x = 2°$ and $L_y = 0.5°$ for the NIO basin, and the obtained results were not sensitive to the decorrelation scales; the results were smoothed by a 0.5° × 0.5° moving average. Moreover, as the biases induced by the algorithm which include the vertical shear errors were relatively small when compared with the mean state (e.g., Qiu et al., 2008), they have not been considered in our study.

We used the 1000 db velocity field derived from the Argo float trajectory data as the reference to construct the absolute geostrophic velocity in each layer using the gridded T/S Argo profile data, following the thermal wind relationship from the surface to 1200 db. The equatorial geostrophic velocities were calculated by following the method under β-plane approximation (Picaut and Tournier, 1991).

2.2. OFES dataset

We utilized the OFES (OGCM for the Earth Simulator; Sasaki et al., 2008) output as a supplement for our observations. The OFES model is forced by the reanalysis wind stress data of 2000–2016 from the National Centers for Environmental Prediction (NECP), and its output is available from the Japan Agency for Marine-Earth Science and Technology (JAMSTEC). The vertical resolution of the OFES model is 58 layers (0−2000m), the spatial resolution is 0.1° × 0.1°, and the temporal resolution is one month.

2.3. Nonlinear $1\frac{1}{2}$-layer reduced-gravity model

In the nonlinear $1\frac{1}{2}$-layer reduced-gravity model, the equations of the upper-ocean can be written as follows:

$$h\frac{\partial u}{\partial t} + h\left(u\frac{\partial u}{\partial x} + v\frac{\partial u}{\partial y}\right) - fhv = -h\frac{\partial E}{\partial x} + hA_h\nabla^2(u) + \frac{\tau^x}{\rho_0} \quad (1)$$

$$h\frac{\partial v}{\partial t} + h\left(u\frac{\partial v}{\partial x} + v\frac{\partial v}{\partial y}\right) + fhu = -h\frac{\partial E}{\partial y} + hA_h\nabla^2(v) + \frac{\tau^y}{\rho_0} \quad (2)$$

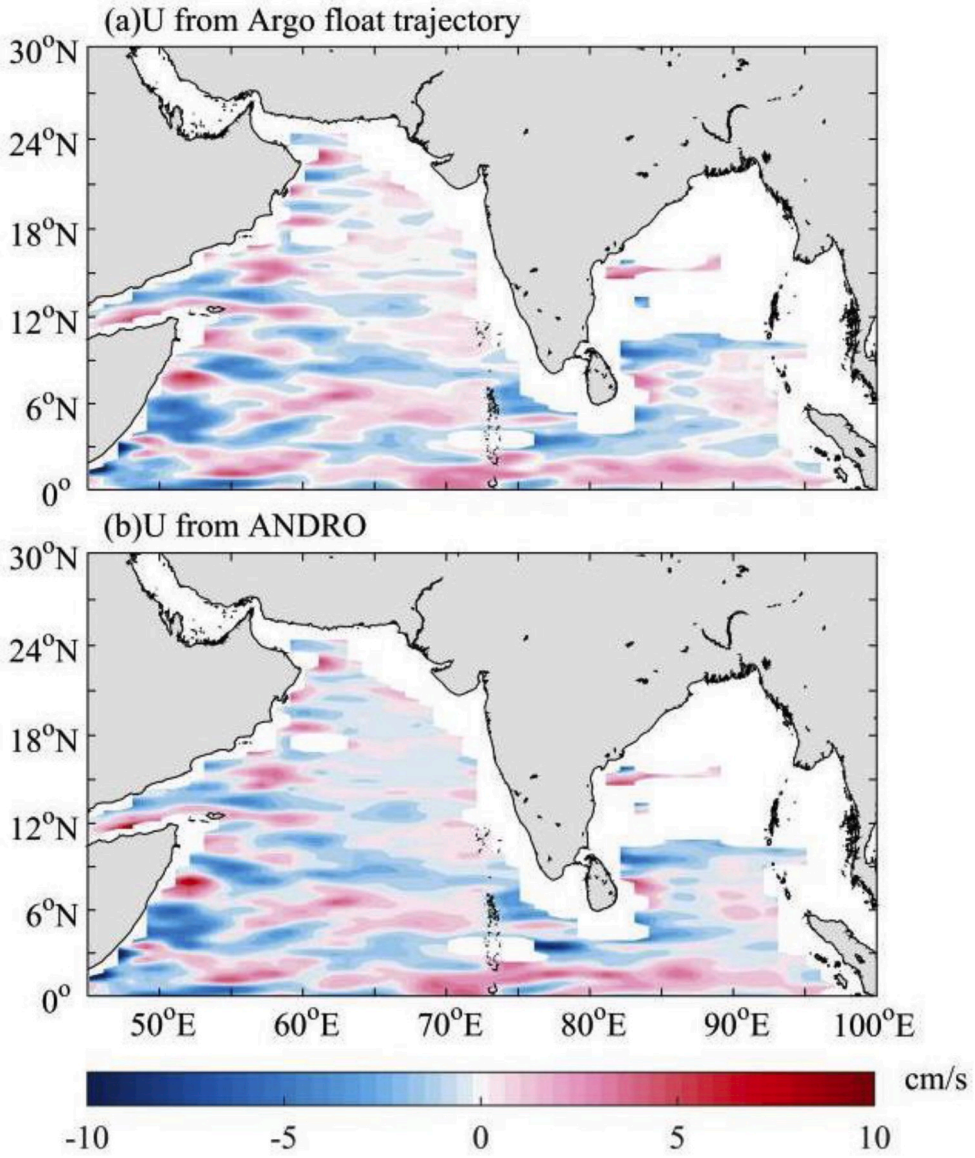

Fig. 3. Time-mean zonal velocity at 1000 db based on (a) Argo float trajectory data and (b) ANDRO dataset from 2002 to 2009.

$$\frac{\partial h}{\partial t}+\left(\frac{\partial hu}{\partial x}+\frac{\partial hv}{\partial y}\right)=0 \tag{3}$$

where h is the thickness of the upper layer; the total energy $E = g^{'}h + (u^2 + v^2)/2$. (u, v) are the upper layer zonal and meridional velocities, respectively, f is the Coriolis parameter; ρ_0 is the reference density; the reduced-gravity constant$g^{'} = \frac{g\Delta\rho}{\rho}$; $(\tau^x, \tau^y)$is the surface wind stress; and A_h is the horizontal eddy viscosity coefficient. Notably, there is no background flow in Equations (1)–(3), and for the absence of an active deep layer, the "nonlinearity" is limited to the Reynolds stresses rather than the stresses due to the density anomalies.

For the model configuration, we set the initial mean upper layer thickness h_0 to 500 m in all experiments, which includes the core depth of the striations in the NIO (see Section 3); the reduced-gravity $g^{'}$was set to a constant value of 0.018 m/s^2. Therefore, $h_0 g^{'} = c^2 = 9\,(m/s)^2$, where c is the speed of the first-mode baroclinic gravity waves; in the tropical Indian Ocean (TIO), the observed c value is approximately 2.6–3.0 m/s (Chelton et al., 1998); besides, the horizontal eddy viscosity A_h was set to 20 m^2/s.

The model is forced by an idealized wind stress, which is expressed as follows: $\tau^x(y,t) = -w_0 \cos\left(\frac{\pi y}{L_y}\right)\cos(\omega_a t)$, where we choose $L_y = 40°$, and the amplitude of the zonal wind stress w_0 is 0.039 N/m^2, which is the averaged amplitude of the wind stress in the equatorial Indian Ocean (10° S–10° N, 40°–130° E). The wind stress domain is in the 5° S–5° N band, with the idealized wind $\tau^x(y,t)$in the 3° S–3° N band; the wind force in the 3°–5° N and 3°–5° S bands smoothly decreases to zero. As the semiannual zonal wind is dominant in the equatorial Indian Ocean (Ogata and Xie, 2011), w_a was set at the semiannual frequency in this study, as already mentioned. The model runs 30 years, at a resolution of 0.25° × 0.25°. The coastline boundary is the only difference in the model settings of the two experiments (see Section 4): the model domain is a simple box from 30°S to 30°N with a zonal width of 100° longitude without coastal geometry (Exp.1). and with a roughly realistic Indian Ocean coastline (Exp.2).

3. Mid-depth striations in the NIO

Fig. 4a shows the zonal component of the mean velocities at the mid-depth 1000 db layer: generally, the striation-like structures are discernible in the equatorial mid-depth region. However, the regular

zonal structure is barely observed in the off-equatorial NIO. The absence of apparent striations in such areas indicates that either there are no band-like structures at all, or the core depth of such jets is not in the 1000 db layer. This could be the reason for the failure of the previous studies to demonstrate the presence of striation-like jets in the off-equatorial NIO.

To test our hypothesis, we examined the vertical structure of the zonal velocities in the western (55°−70°E) and eastern subdomains (80°−95°E) (Fig. 4b and c). For the western subdomain, the eight eastward flows are located at 2° N, 6° N, 9.5° N, 12.5° N, 15.5° N, 17.5° N, 19.5° N, and 23° N, with a meridional scale ~300 km. To better illustrate the alternating structures, we plotted the high-pass filtered velocity (Fig. 4d and e): we observe that compared with the unfiltered velocity, the locations of the eight eastward flows in Fig. 4c and d are consistent with those in Fig. 4d and e. Moreover, Fig. 4d and e shows two more hidden bands at 4.5° N and 21° N. In comparison, the typical meridional scale for the striations in the North Pacific Ocean is ~450 km (Qiu et al., 2013a, b). Thus, we observe that the meridional scale of the

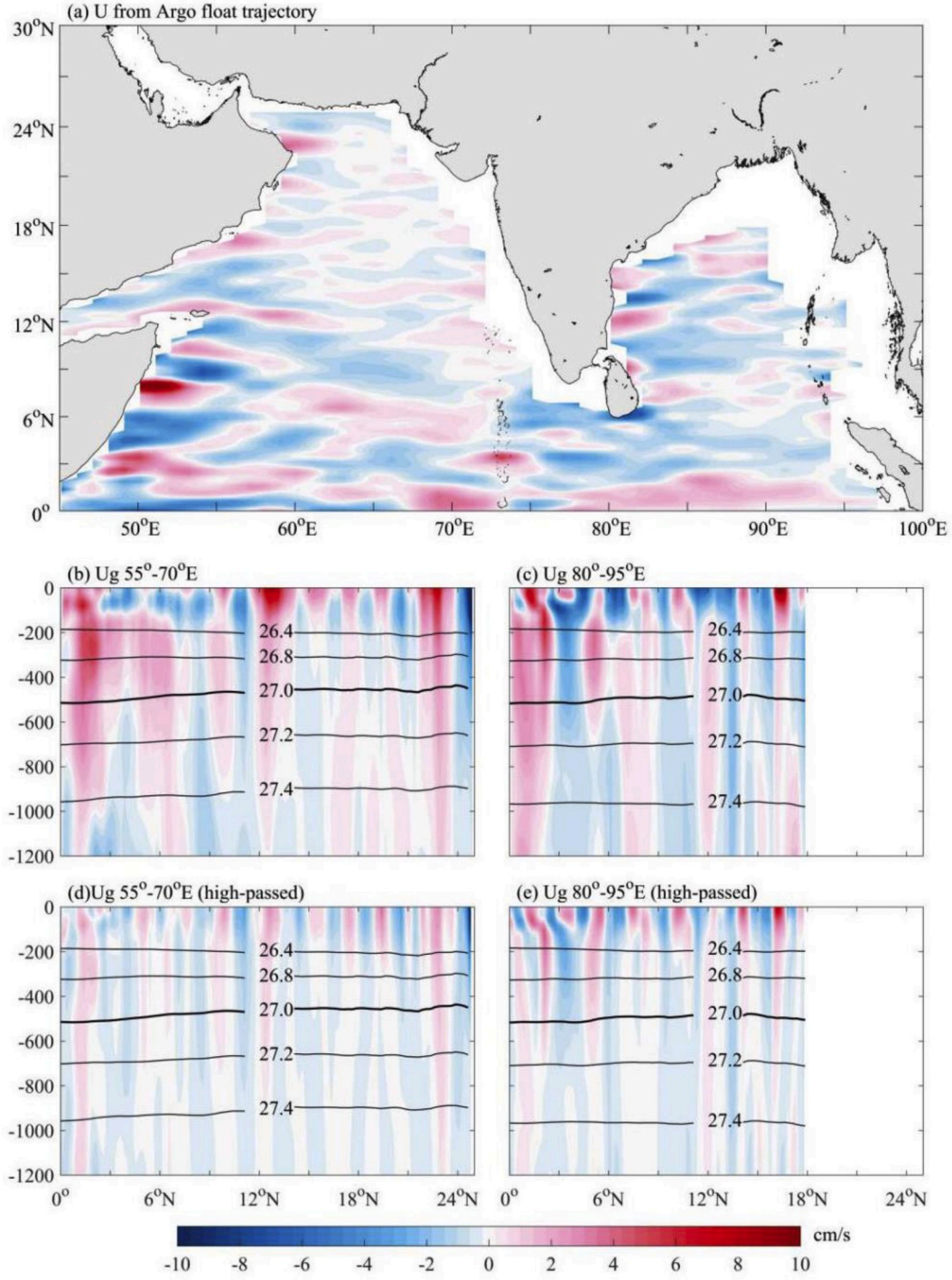

Fig. 4. Time-mean zonal velocity of the NIO during 2004–2016. (a) 1000 db zonal velocity based on Argo float trajectory data. Boxes with less than three data points are blanked. Mean geostrophic zonal currents were zonally averaged in (b) 55°–70°E and (c) 80°–95° E bands as a function of depth and latitude. (d) and (e): same as (b) and (d), but for the high-pass filtered (4°-box moving averaged) velocity; the depth is ranged from 0 to 1200 m. The black lines denote isopycnals from 26.4 to 27.4 kg/m^3.

NIO striations is much narrower. The time-mean zonal velocity of these jets is about 2cm/s, and the core depth is above the 500 db layer, which is consistent with our hypothesis. However, the Bay of Bengal does not exhibit clear band-like structures.

Fig. 5a displays the zonal currents on the 27.0 kg/m^3 isopycnal. Compared with Fig. 4a, the striation-like structures are clearer in the Arabian Sea. Fig. 5b shows the zonally averaged zonal velocity over 60°−70°E. The locations of the eastward/westward jets derived by the OFES simulation are consistent with the Argo observations.

Based on the characteristics of the mid-depth currents in the NIO, the following two questions commonly arise:

i) What controls the meridional scale of the observed striations?
ii) What determines the distribution of the mid-depth striations? For example, why are the striations prominent in the Arabian Sea but barely observed in the Bay of Bengal?

4. Discussion

4.1. Results from the nonlinear $1\frac{1}{2}$-layer reduced-gravity model

The nonlinear $1\frac{1}{2}$-layer reduced-gravity model could quantitatively simulate the first baroclinic mode response of the upper layer ocean, and has been successfully used to explore the formation mechanisms of the North Pacific Ocean striations (Qiu et al., 2013b). Therefore, to evaluate the vertical structure in the NIO, we calculated the first baroclinic mode in the NIO (Fig. 6a) by solving the eigenvalue problem $\frac{d\left(\frac{f^2 d\Phi}{N^2 dz}\right)}{dz} - \left(\frac{\beta}{c}\right)\Phi = 0$, for the condition: $\frac{d\Phi}{dz} = 0$ at $z = 0$ and $\Phi = 0$ at $z = -H$, where H is the ocean depth, N^2 is the squared buoyancy frequency. β is the meridional gradient of the Coriolis parameter, and c is the speed of the first-mode baroclinic gravity waves. The regression coefficients of the zonal velocity anomalies (here, the anomalies are relative to the time mean) against those at 500m depth based on the OFES simulation are shown in Fig. 6b. The OFES-simulated vertical structures of the zonal velocity anomalies are qualitatively similar to those of the first baroclinic mode. Hence, this result justifies the use of the nonlinear $1\frac{1}{2}$-layer reduced-gravity model for exploring the basic dynamics of the NIO striations.

To clarify the factors that control the meridional scale of the NIO striations, it is instructive to individually address the following two issues: (i) the frequency of the surface wind forcing, and (ii) the detailed coastline geometry. Unlike the other ocean basins, the equatorial NIO is subject to significant seasonal variations in monsoon wind forcing, while the eastern coastline geometry might affect the release of the baroclinic Rossby waves. Besides, the relatively narrower width of the equatorial Indian Ocean, compared with the Pacific Ocean could significantly influence the wave interactions under the external wind stress forcing.

Fig. 7a shows the averaged zonal velocity over last 10-years. The eastward zonal velocities are located at 8° N, 12° N, 16° N, 20° N, and 24° N in the northern hemisphere, and the meridional scale of the striations is approximately 400 km, which is larger than the observed scale. Fig. 7b shows the snapshot of the upper layer thickness anomalies in the last model year, wherein the breakdown of the semiannual Rossby waves into eddies can be observed. The difference in the meridional scale of the striations between Exp.1 and the Argo observations suggests that the semiannual period of wind stress forcing does not significantly influence the meridional scale. However, the zonal width between the locations of the eddy generation and the eastern boundary is shrunk, compared with the result of Qiu et al. (Fig. 8b in Qiu et al., 2013b). In other words, the narrower width between the Rossby wave breakdown line and the eastern boundary may be due to the semiannual wind stress forcing: If the width between the Rossby wave breakdown line and the eastern boundary was larger than the basin width, the Rossby waves travel across the whole basin rather than break into eddies; hence, the eddy-driven jets would not exist. The NIO basin width is relatively narrower, especially where the Bay of Bengal and the Arabian Sea are separated by the Indian subcontinent. Thus, the semiannual period of wind stress is important for the NIO striations.

The time-mean zonal velocity of Exp. 2 is shown in Fig. 8a and the strength is roughly half that of Exp. 1. We observe that the meridional scale of the modeled striations becomes smaller, and is reduced to ~300

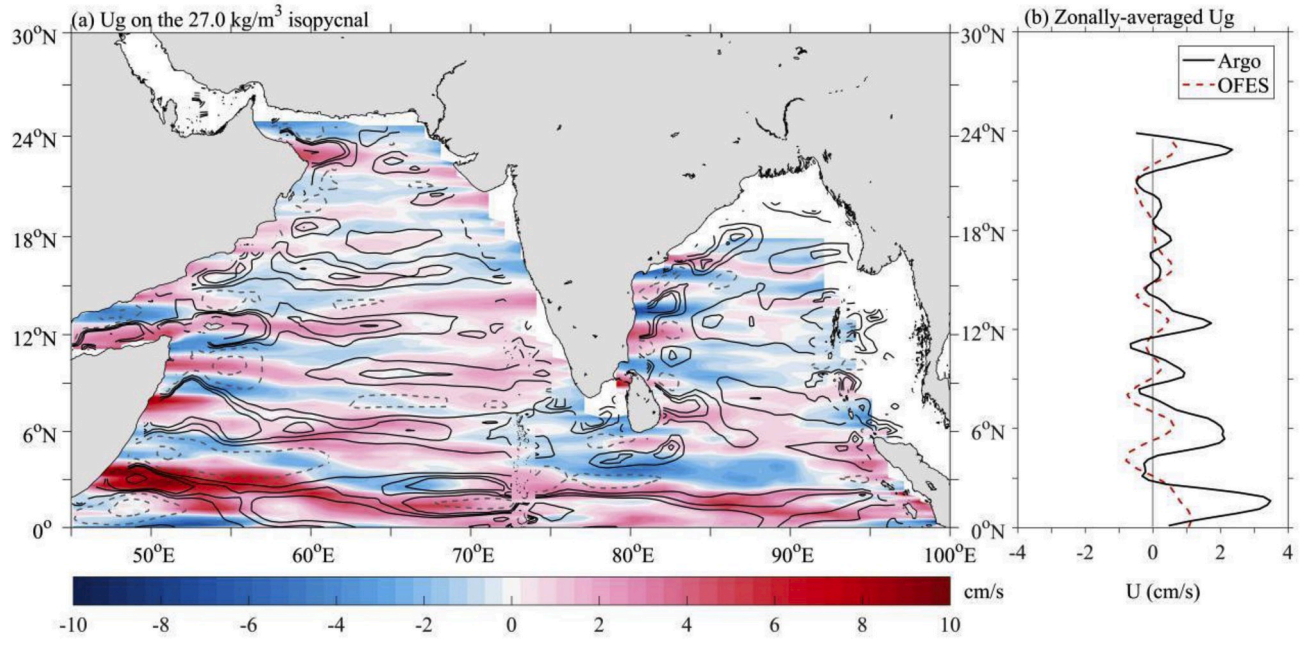

Fig. 5. Time-mean zonal velocity on the 27.0 kg/m^3 isopycnal (~500 db) averaged from 2004 to 2016. (a) The zonal velocity from the OFES simulations (contours, solid/dashed lines present eastward/westward flows) and derived from the Argo T/S data with the reference layer velocities on the 1000 db from the Argo float trajectory product (color shaded region). (b) Comparison of the zonally-averaged zonal velocity over 60°−70°E from the Argo floats (dashed red line) and the OFES simulation (solid black line) in (a).

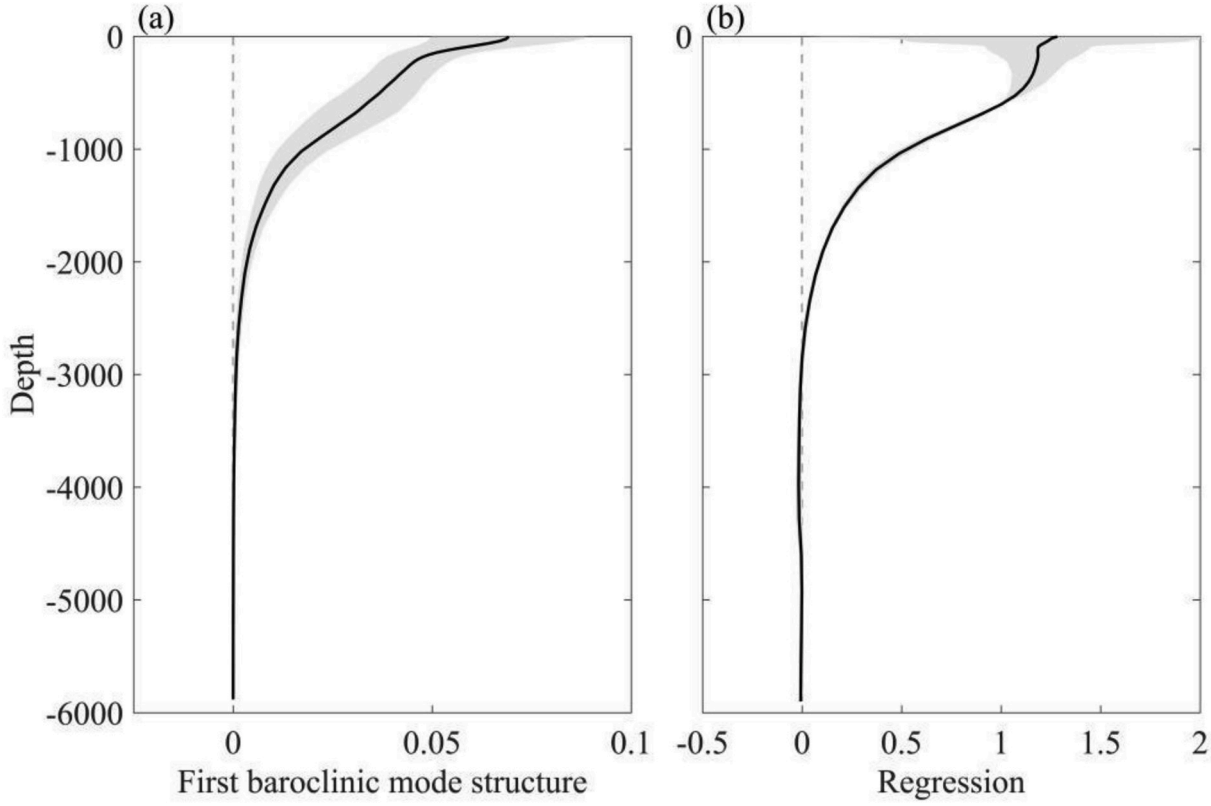

Fig. 6. Vertical structure of (a) first baroclinic mode profile, and (b) regression coefficient of the zonal velocity anomalies against those at the 500 m depth. The solid lines represent the domain-averaged values, and the shades denote the standard deviations—all averaged in the NIO (5°–25° N, 45°–100° E) during 2000–2016 based on the OFES simulations.

km; the striation-like zonal currents in the NIO appear to exist only in the latitudes of 4° N, 7° N, 9.5° N, 12.5° N, 15.5° N, and 18.5° N (relatively weaker) in the western Arabian Sea (see Figs. 8a and 9b for a better view). In contrast, no clear quasi-zonal jet structure is observed in the Bay of Bengal, in accordance with the OFES simulations and Argo observations. The following discussion reveals that the lack of striations in the Bay of Bengal is due to its narrower zonal basin than the distance between the Rossby wave breakdown line and eastern boundary. Fig. 8b shows the snapshot of the upper layer thickness anomalies of the model used in Exp.2, which reveals that the semiannual Rossby waves break down to eddies in the Arabian Sea rather than in the Bay of Bengal.

The snapshots of the upper layer thickness anomalies from Exp.1 and Exp.2 show the eddies in the west of the breakdown line (see Figs. 7b and 8b). The generation of striations is explained as follows: As detailed in Qiu et al. (2013b), the convergence of the eddy potential vorticity fluxes contributes to the mean flow across the mean potential vorticity gradient (turbulent Sverdrup balance, Rhines and Holland, 1979). The potential vorticity Q is Lagrangian conserved, such that $\overline{\boldsymbol{u}}\cdot\nabla\overline{Q} = -\overline{\boldsymbol{u}'\cdot\nabla Q'}$, where $Q = (f + k\cdot\nabla\times u)/H$. Compared with $\frac{\partial Q}{\partial y}$, $\frac{\partial Q}{\partial x}$ is nearly zero; thus, $\overline{\boldsymbol{u}}\cdot\nabla\overline{Q} = \overline{v}\frac{\partial\overline{Q}}{\partial y}$. Once $\overline{v}$is determined, $\overline{u}$ can be estimated from the time-mean continuity equation. Fig. 9a shows that time-mean zonal velocity derived from turbulent Sverdrup balance, which agrees well with the result derived from Exp.2, suggesting that the striations are formed by the convergence of the potential vorticity fluxes associated with these eddies.

Fig. 9b presents a comparison of the zonally averaged velocity derived from the Argo observations, OFES simulations, Exp.2, and the turbulent Sverdrup balance: We observe that although the location (latitude) of one of the westward flows at 12° N from the Exp.2 output is slightly higher than those from the observations, the other locations of the alternating eastward/westward velocity are roughly consistent with the observations toward the south of 16° N. However, the magnitude of the velocity from the OFES simulations and Exp.2 is smaller than those from the Argo observations.

We further observe that the PV gradient inhomogeneity results not only from the meridional variation of the Coriolis parameter but also from the bottom topography, larger-scale background circulation, varying vertical stratification, and Reynolds number (Berloff and Kamenkovich, 2013a, b). However, compared with the Rossby wave phase speed (7–30 cm/s), the speed of the eastward/westward flows is relatively small (1–2 cm/s). Fig. 4d and e shows the vertical structures of the zonal velocities after the high-pass filtered and mid-depth striations extend vertically to the surface. Hence, as we have not considered the background currents and inhomogeneous stratification in this study, the PV gradient inhomogeneity results from the nonlinear interactions of the eddies.

Qiu et al. (2013b) revealed a mechanism for the generation of zonal jets in the North Pacific by triad baroclinic Rossby wave interactions. Through the unstable triad Rossby wave interactions, the primary baroclinic Rossby waves break down to eddies and then generate the eddy-driven zonally averaged jets. The result of Exp.2 also suggests that the meridional scale of the striations in the Arabian Sea may also satisfy the triad Rossby wave interaction theory, although the Indian subcontinent is located in the middle of the NIO basin blocking the baroclinic Rossby waves traveling directly across the NIO basin from the eastern boundary. In the near-equatorial region, there is another eastward flow located at 2° N according to the Argo observations. However, in Exp.2, the eastward flows are located on the equator (unstable) and 4° N—the meridional scale in the near equatorial region is slightly larger than that in the Arabian Sea. To clarify the dynamics of the striations in the Arabian Sea, we used the nonlinear $1\frac{1}{2}$-layer reduced-gravity model and specified Exp. 2 with an idealized coastline. Furthermore, we hypothesized that the wind-forced equatorial Kelvin wave signals propagate to

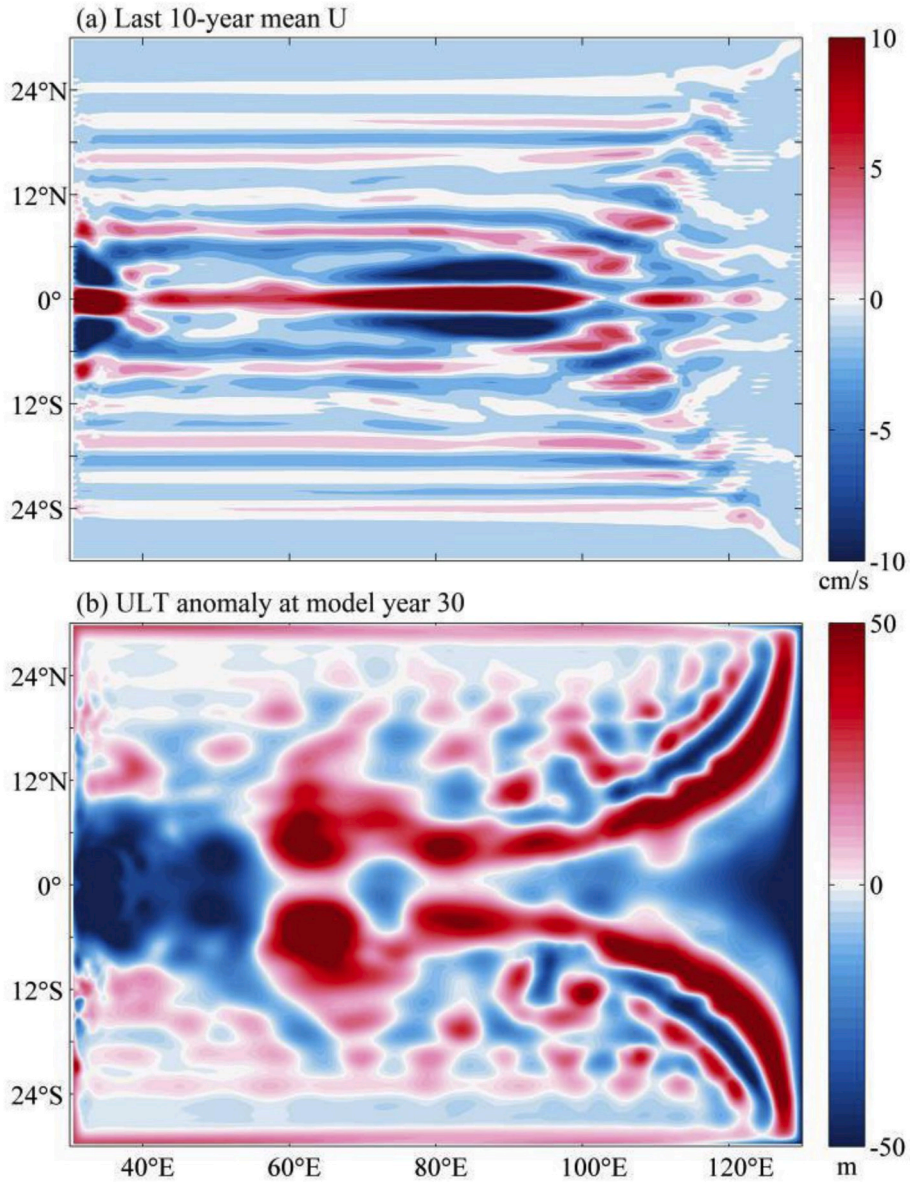

Fig. 7. Result obtained from the nonlinear $1\frac{1}{2}$-layer reduced-gravity model with a simple box coastline (Exp.1). (a) Time-mean zonal velocity, averaged from the model years 20–30; (b) snapshot of the upper layer thickness anomalies at the model year 30.

the eastern boundary of the Arabian Sea via the coastal trapped Kelvin waves and then shed the westward propagating Rossby waves. Fig. 10a presents the locations of the stations along this waveguide. In Fig. 10b, we plotted the time-station diagram of the lead-lag regression of the last eight-year modeled upper layer thickness anomalies along the station locations. The wave phase speed along the coastline is estimated to be approximately 2.8m/s, which is consistent with the first-mode baroclinic Kelvin wave phase speed (2.6–3.0m/s; Chelton et al., 1998; Cheng et al., 2013).

To examine the sensitivity of the horizontal eddy viscosity coefficient, we repeated Exp.2 with increased A_h values, namely 50 and 100 m^2/s, and the results of the time-mean zonal flows are shown in Fig. 11a and b. We observe that the model domain in Fig. 11 is the same as that in Exp.2, except that Fig. 11 only shows the time-mean zonal velocity in the Arabian Sea. The meridional scale of the striations is similar to the results of Exp.2, although with a relatively weaker strength. However, Qiu et al. (2013b; Fig. 16 in their published work) proved that A_h is insensitive to the meridional wavelength.

Furthermore, we repeated Exp.2 with increased and decreased wind forcing amplitudes (namely 0.078 and 0.0195 N/m^2, as shown in Fig. 11c and d, respectively). The meridional scale of the striations appears larger in Fig. 11c. Although the eastward flow located at 7° N is very weak, there are three eastward flows in the 6°–18° N band. On the other hand, in Fig. 11d, there are four eastward flows in the same band, which is similar to Fig. 8a. However, the eastward flow located at 6.5°N is much clearer. The meridional scale of the striations is sensitive to the wind force stress, and the temporal variability of the striations can be also impacted by eddy trains and varying bottom topography (Khatri and Berloff, 2019; Chen et al., 2016). Note that we have only used the time-mean observations and OFES simulations to reveal the NIO striations; therefore, the transient feature of the striation-like structures is beyond the scope of this paper.

4.2. Triad baroclinic rossby wave interaction

Although the results from Exp.1 and Exp.2 suggest that the narrower meridional scale of the NIO striations is sensitive to the specific coastline geometry, the dynamic mechanism remains to be clarified. Moreover,

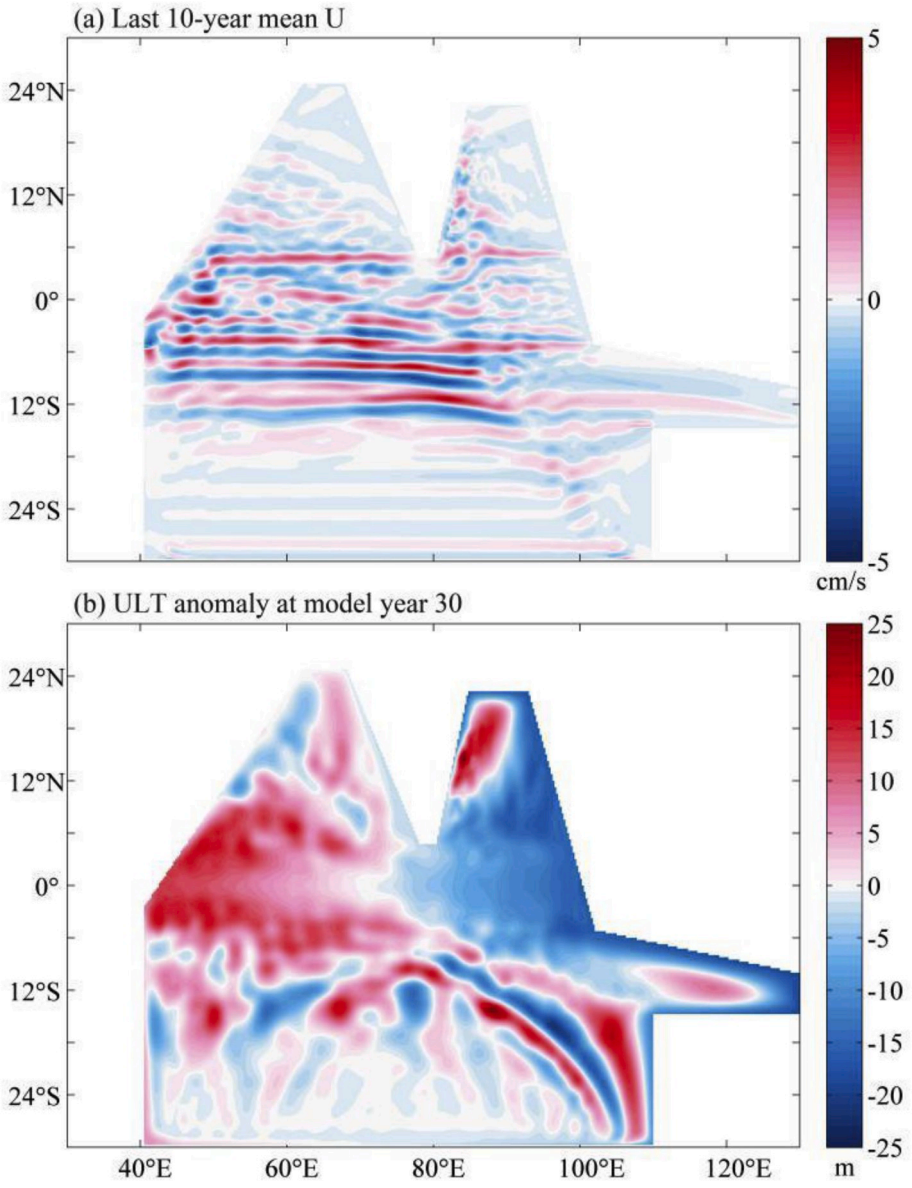

Fig. 8. Same as Fig. 7, but with an idealized coastline (Exp. 2).

while the complex coastline obviously plays a crucial role in the generation of the striations, the extent to which it can quantitatively determine their meridional scale needs consideration. For this, there are two potential factors that can be considered as relevant: First, the angle of the coastline boundary may impact the shedding of the baroclinic Rossby waves that could control the wave ray path and subsequently determine the meridional scales of the striations. Second, the basin width in the equatorial region in Exp.2 is much smaller than that in Exp.1 (cf. Figs. 7a and 8a), which means that the wind stress forcing is applied over a smaller area in Exp.2 than in Exp.1; therefore, the wind-forced equatorial Kelvin waves are weaker in Exp.2. As we have used the zonally uniform wind force in the model, the wind-forced energy input is directly proportional to the basin width along the equator; i.e., the smaller basin scale may be regarded as a case with weaker wind stress forcing, and the wind stress is sensitive to the meridional scale of the striations, as indicated in Fig. 11c and d.

To better understand the generation dynamics of the NIO striations as well as to clarify the critical factors responsible for their smaller meridional scale, we herein adopted the triad baroclinic Rossby wave interactions theory (Pedlosky, 1987), which explains the dynamics of the wave breakdown. The superposition of the Rossby waves is not a linear process but a nonlinear interaction between these waves, which leads to a nonlinear coupling and energy transportation. Then, the primary baroclinic Rossby waves carry energy along the ray path to the equatorial region. Furthermore, using the baroclinic Rossby wave ray path theory (Schopf et al., 1981) combined with the no mean flow assumption, low-frequency wave approximation, and β-plane approximation, the solutions for the meridional eastern boundary (as in Exp.1) can be expressed as follows:

$$\theta = \frac{-2\omega^2 t}{kc} \tag{4}$$

$$y_T^2 = y_0^2 + \frac{l_0^2 c^2}{\beta^2} \tag{5}$$

$$x = x_0 - \frac{c}{2\omega}\left(1 - \frac{4\omega^2}{c^2} y_T^2\right)\theta \tag{6}$$

$$y = y_T \cos(\theta + \theta_0) \tag{7}$$

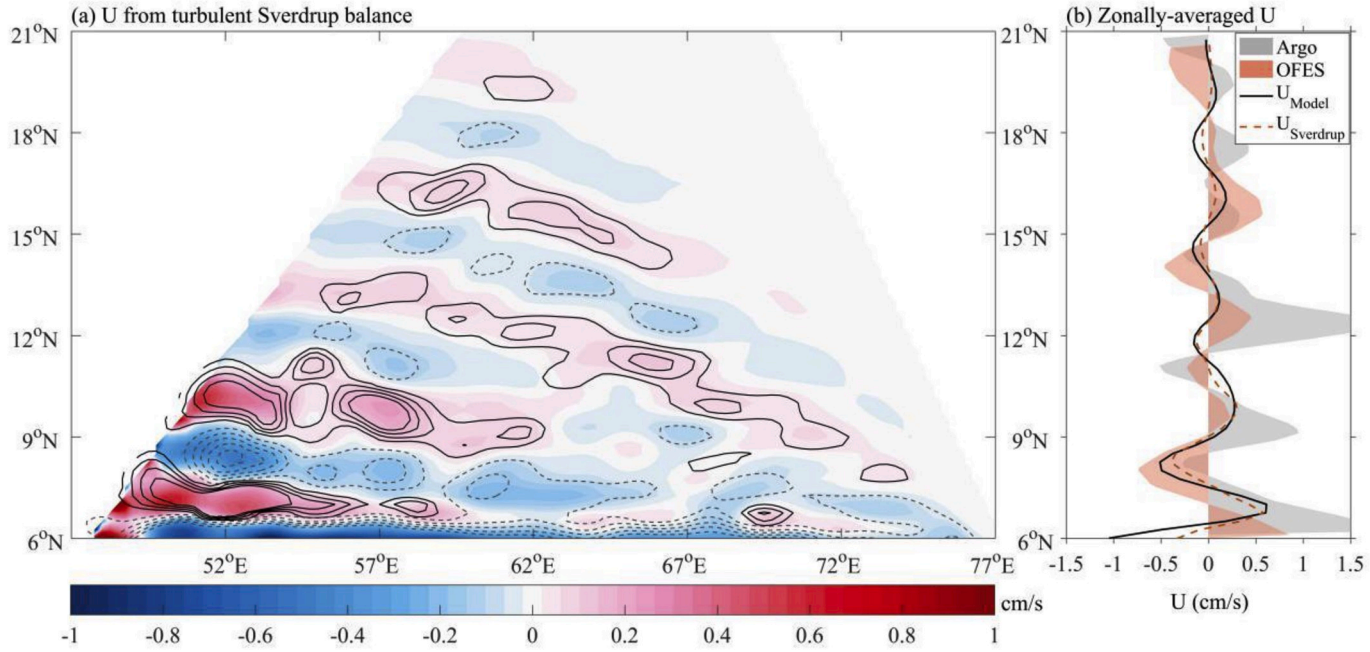

Fig. 9. Comparison of the time-mean zonal velocity from Exp.2, OFES simulations and Argo observations. (a) Time-mean zonal velocity calculated from the turbulent Sverdrup balance in Exp.2 (color shaded region) and Exp.2 output (contours, solid/dashed lines present eastward/westward flows). (b) Zonally averaged zonal velocity derived from the model result (solid black line) and the turbulent Sverdrup balance (dashed red line), the averaged area is offshore (from the western boundary) 5° band. The zonally averaged zonal velocities over 60°−70°E are from the Argo floats (gray shadowed region) and the OFES simulation in Fig. 5a (orange shadowed region).

$$l = \frac{\beta}{c} y_T \sin(\theta + \theta_0) \tag{8}$$

$$\theta_0 = \begin{cases} \cos^{-1}\left(\frac{y_0}{|y_T|}\right) & if\ l_0 > 0 \\ -\cos^{-1}\left(\frac{y_0}{|y_T|}\right) & if\ l_0 < 0 \end{cases} \tag{9}$$

here x and y are the locations of the baroclinic Rossby wave ray path; θ is the phase of the baroclinic Rossby wave, which changes with time t; the subscript 0 refers to the initial values of x, y, l, and θ; c is the phase speed of the baroclinic Rossby wave, ω is the frequency of the baroclinic Rossby wave; k and l are the zonal and meridional wave numbers of the baroclinic Rossby wave, respectively, and y_T is the maximum latitude of the Rossby wave energy along this particular ray. Compared with the Rossby waves, the coastal trapped Kelvin waves travel much faster, which implies that the Rossby waves are released almost simultaneously from the eastern boundary. To simplify these equations, we assumed that the wave amplitude and phase are uniform along the eastern boundary. As there is a meridional boundary, the waves released from the eastern boundary satisfy the conditions: $l_0 = 0$, $y_T = y_0$, and $\theta_0 = 0$. Using these equations, the ray path of a semiannual baroclinic Rossby wave with different y_0 values has been plotted in Fig. 12a.

For a non-meridional coastline (as in Exp.2), the wavenumber vector $\boldsymbol{k}$ must satisfy $\boldsymbol{k}\cdot\boldsymbol{e}_s = l_s$, where $\boldsymbol{e}_s$ is a unit vector along the coast, and l_s is the alongshore component of the wavenumber vector (Schopf et al., 1981). Again, assuming uniform wave amplitude and phase along the eastern boundary ($l_s = 0$), we have:

$$k_0 = -\frac{\beta cos^2\alpha}{2\omega}\left[1 - \left(1 - \frac{4\omega^2 y_0^2}{c^2 \cos^2\alpha}\right)^{\frac{1}{2}}\right] \tag{10}$$

$$l_0 = -k_0 \tan\alpha \tag{11}$$

$$x_0 = y_0 \tan\alpha \tag{12}$$

where the subscript 0 refers to the initial values of the zonal and meridional wavenumbers k and l and the initial values of x and y. k , l, x, y, c, ω, and β are the same as in Equations (4)–(9); and α is the coastline angle relative to the North. Equation (10) suggests that the Rossby waves emanating from the eastern boundary must satisfy $1 - \frac{4\omega^2 y_0^2}{c^2\cos^2\alpha} > 0$, and the latitude of the propagating Rossby waves cannot be higher than $y_{max} = \frac{c\cos\alpha}{2\omega}$. Furthermore, we observe that y_{max} indicates the maximum latitude along the eastern boundary, while y_T is the maximum latitude of the Rossby wave energy along a particular ray path. In Fig. 13c, for example, $y_{max}$is 23.6°, with the eastern boundary having an angle $\alpha = 45°$ (Exp.2); in Exp.1, where $\alpha = 0$, y_{max} is 33.6°.

The model results indicate that the striations are generated by the breakdown of the semiannual baroclinic Rossby waves. As detailed in Pedlosky (1987), the quasi-geostrophic stream function can be written as:$\psi = \psi_0 + \varepsilon\psi_1 + \varepsilon^2\psi_2 \ldots$, where $\varepsilon = U/\beta L^2$ by using the method of multiple time scales. At $o(0)$, the solution of the quasi-geostrophic potential vorticity equation can be regarded as a linear superposition of the primary semiannual baroclinic Rossby waves and the instability-generating secondary baroclinic Rossby waves, which have a much smaller amplitude than the primary waves. However, at $o(1)$, $\varepsilon\psi_1$ represents the nonlinear wave interactions. When resonance occurs, the magnitude of $\varepsilon\psi_1$ is as large as ψ_0, and therefore, the nonlinear interaction is important for the solution. Along these ray paths of the semiannual baroclinic Rossby waves, the zonal wavenumber k_2 and wave frequency $\omega_2$of the baroclinic Rossby waves are constant, owing to the unaltered background mean state. As the baroclinic Rossby waves propagate westward, their meridional wave number l_2 increases according to Equation (8), and the primary waves interact with secondary baroclinic Rossby waves with the growth rate rapidly increasing. As detailed by Qiu et al. (2013b), we can acquire the wavenumber of the secondary waves (l_1, l_3, k_1, k_3) by the following triad wave interaction relationship:

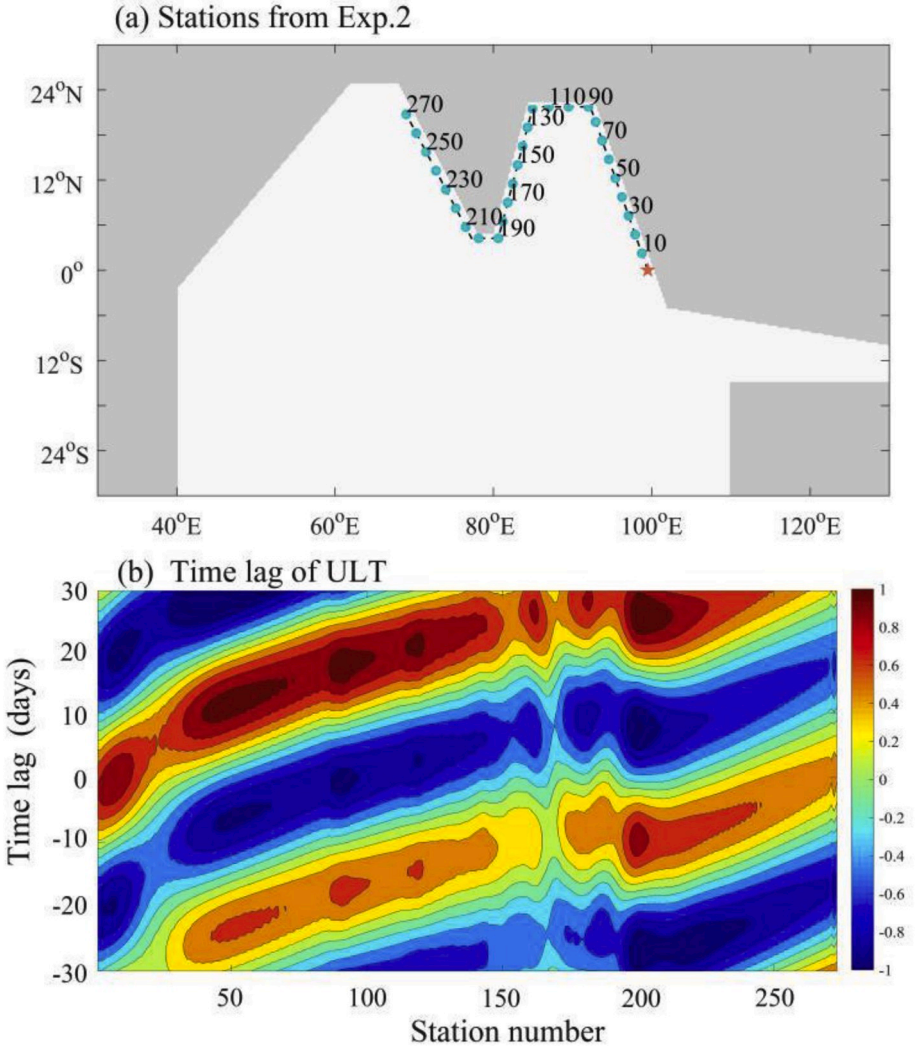

Fig. 10. The lead-lag regression of the modeled upper layer thickness anomalies in the last eight-years along the station locations. (a) Distribution of stations along the NIO coast. (b) Corresponding time-station lag regression of the model upper layer thickness with respect to the equatorial model upper layer thickness at the stations indicated by the blue dots; the red star is taken as the reference time series. The upper layer thickness has been high-pass filtered with a half-power at 30–60 days.

$$k_1 + k_2 + k_3 = 0 \tag{13}$$

$$l_1 + l_2 + l_3 = 0 \tag{14}$$

$$\sigma_1 + \sigma_2 + \sigma_3 = 0 \tag{15}$$

Where$\sigma$is the frequency of the primary and secondary waves, and is given by the linear Rossby dispersion relationship: $\sigma_n = \frac{k_n}{k_n^2 + l_n^2 + F}$ (n = 1, 2, 3), where $F = \frac{f^2}{g' h_0}$ (or $\frac{1}{L_d^2}$) is the reciprocal of the square of the baroclinic deformation radius L_d (Pedlosky, 1987). The potential enstrophy is proportional to the wavenumbers. Thus, constrained by the conservation of energy and enstrophy, the secondary wavenumbers must satisfy the condition: $K_1 < K_2 < K_3$, where $K_n^2 = k_n^2 + l_n^2$ (n = 1, 2, 3).

As detailed in Pedlosky (1987) and Qiu et al. (2013b), the growth rate of the instability-generating secondary waves can be derived as $\lambda = A_2 \left[\frac{B(K_2,K_3)B(K_1,K_2)}{(K_1^2+F)(K_3^2+F)} \right]^{1/2}$, where the interaction coefficient $B(K_m, K_n) = (K_m^2 - K_n^2)(k_m l_n - k_n l_m)$ (n = 1, 2, 3 and m = 1, 2, 3), and the amplitude of the primary wave $A_2 = \frac{g'}{f} h_a$, where h_a is the amplitude of the upper-layer thickness anomalies along the eastern boundary (see Qiu et al., 2013b for more details). As shown in Fig. 12b, there are a series of possible results for the unstable secondary Rossby waves: when the growth rate is maximum, the triad wave interaction has the highest probability of occurrence, and the primary Rossby waves feed their energy to the secondary waves. The most unstable secondary wave dominates the meridional scale of the eddies. The eddies induce the time-mean zonal jets through nonlinear interaction; in this case, the meridional scale of the striations is consistent with the shorter secondary wavelength L_{y3} = 300 km rather than larger secondary wavelength L_{y1} = 750 km. Qiu et al. (2013b) proved that owing to the conservation of both kinetic energy and enstrophy, the three baroclinic waves satisfy $L_{y1} > L_{y2} > L_{y3}$. Moreover, because of their larger spatial scales, the larger secondary unstable waves are not dynamically effective in forming the time-mean flow. The turbulent Sverdrup balance requires eddy PV flux convergence to form the zonal-mean jet: this convergence will necessarily be small for large-scale eddy flows. Thus, it is the meridional wavenumber l_3 of the most unstable shorter secondary waves (located outside the red circle, i.e., $k_3 \sim 2 \times 10^{-6}$ m^{-1} and $l_3 \sim -2 \times 10^{-5}$ m^{-1}, corresponding to $L_{x3} \sim$ 3000 km and $L_{y3} \sim$ 300 km, respectively) that controls the meridional scale of the instability rather than that of the most unstable, longer secondary waves (located outside the circle, i.e., $k_1 \sim 3.5 \times 10^{-6}$ m^{-1} and $l_1 \sim 9 \times 10^{-6}$ m^{-1}, corresponding to $L_{x1} \sim$ 2000 km and $L_{y1} \sim$ 700

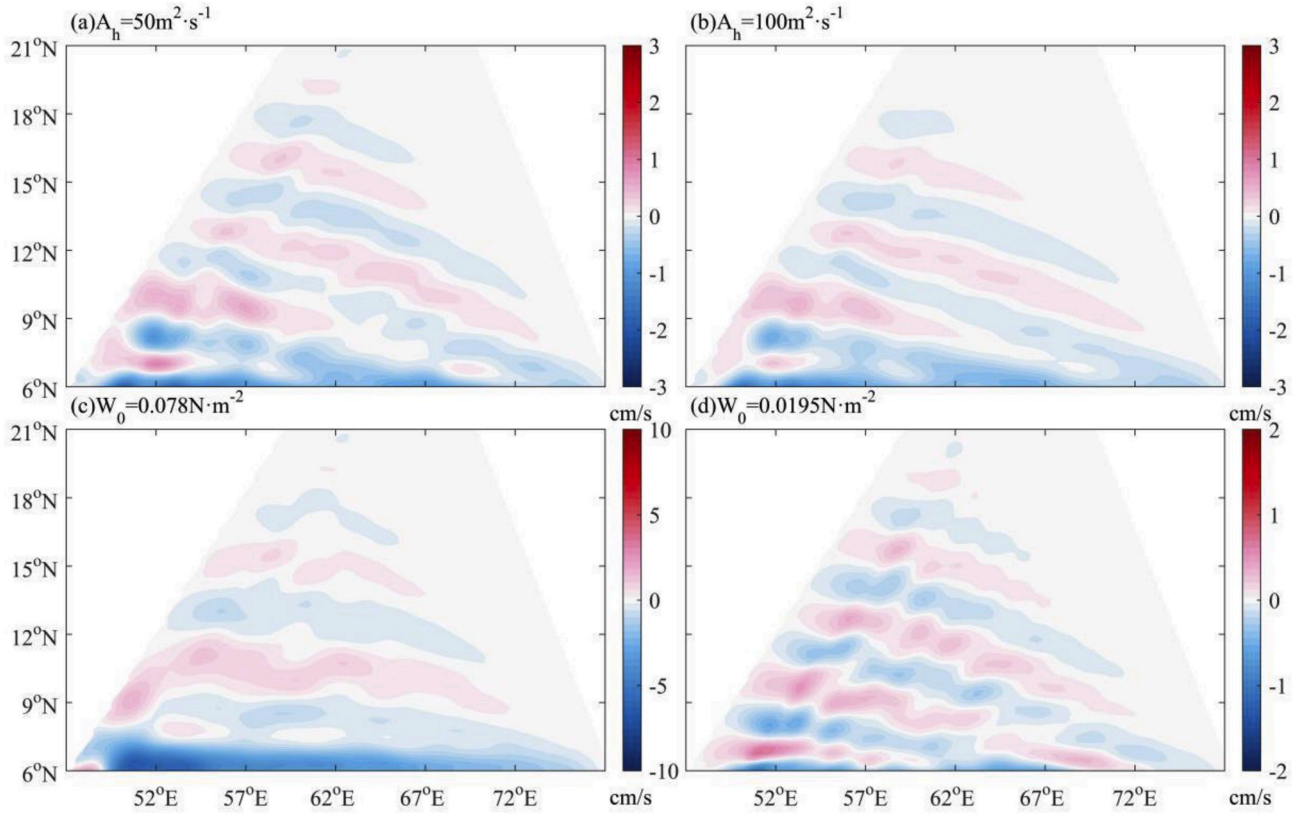

Fig. 11. Time-mean zonal velocity averaged from the model year 20–30 in the Arabian Sea from the nonlinear $1\frac{1}{2}$-layer reduced-gravity model that has an increased horizontal eddy viscosity coefficient: (a) $A_h = 50$ m^2/s and (b) $A_h = 100$ m^2/s (c) A double wind forcing amplitude $w_0 = 0.078$ N/m^2, and (d) a half wind forcing amplitude $w_0 = 0.0195$ N/m^2. Notably, the scales in the color bar are different from those in Fig. 8a.

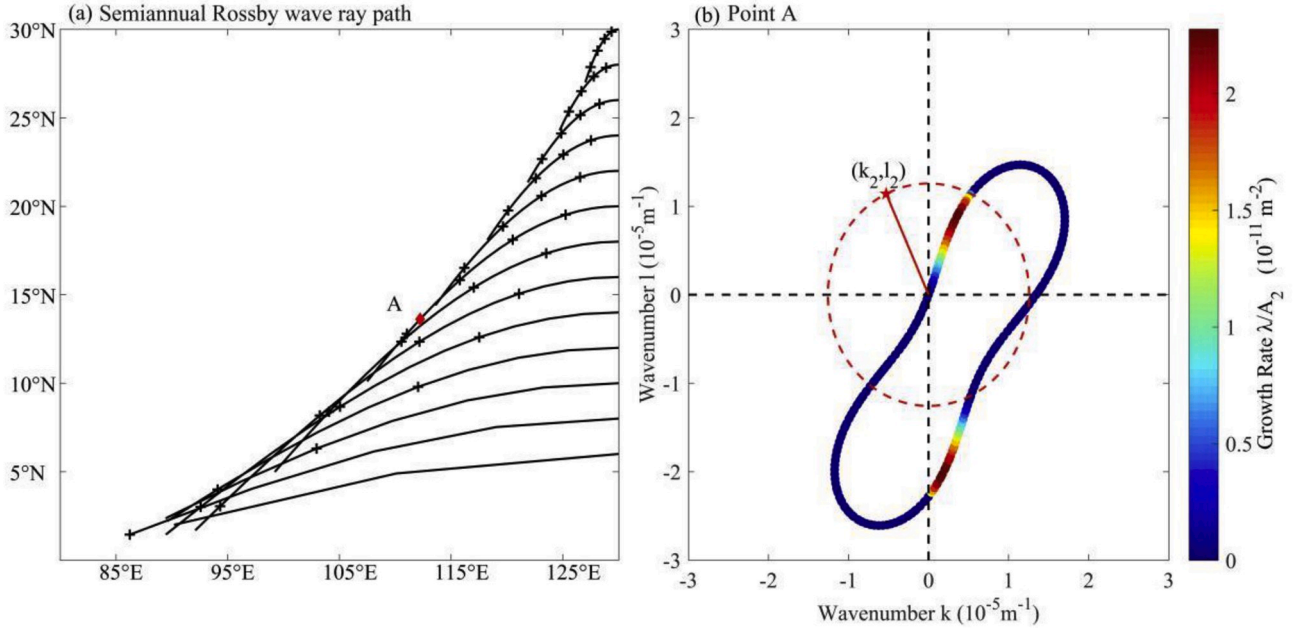

Fig. 12. Analytical ray paths and wavenumbers of the semiannual Rossby waves. (a) Analytical ray paths for the semiannual baroclinic Rossby waves (as in Exp.1) under the assumption of uniform wave amplitude and phase along the eastern boundary (also see Fig. 4 in Schopf et al., 1981). The plus symbols indicate a three-month interval along each path. (b) Vector (k_2, l_2) indicates the primary semiannual Rossby wave at location A. The discrete dots represent all possible secondary wavenumbers satisfying the triad wave interactions, the red dashed circle corresponds to $K = K_2$, and the colors indicate the value of the growth rate.

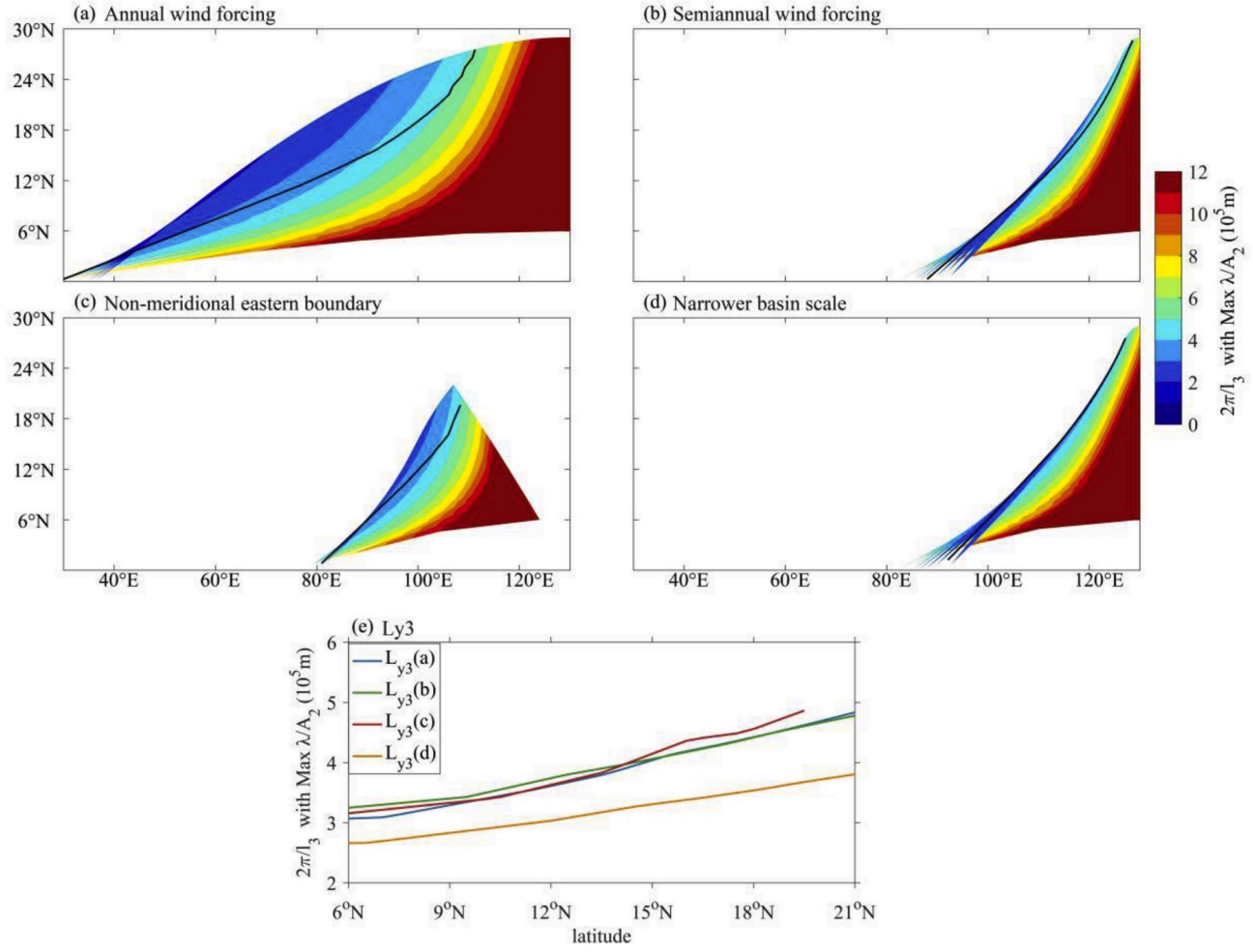

Fig. 13. Analytical spatial distribution of the meridional scale for the most unstable secondary wave along the primary Rossby wave ray paths in four different cases. The solid lines denote the location of the e-folding time scale of the most unstable triad instability that matches the advective time scale of the primary waves. (a) Annual wind forcing, the meridional eastern boundary, large basin zonal extent (100°); (b) same as (a) but for semiannual wind forcing; (c) semiannual wind forcing, northwest-southeast oriented eastern boundary ($\alpha = -45°$), large basin zonal extent; and (d) semiannual wind forcing, meridional eastern boundary, narrower basin zonal extent (60°). (e) Meridional scale for the most unstable shorter secondary wave as a function of latitude, and the legends (a–d) are same as in (a)–(d).

km, respectively) (Qiu et al., 2013b).

The primary waves propagate to the west with the advective time scale $\frac{2\pi}{K_2 c_g}$, where c_g is the associated group velocity. When the advective time scale of the primary wave becomes equal to the e-folding time scale of the most unstable short secondary wave λ^{-1}, the primary baroclinic Rossby waves break down to nonlinear eddies. These nonlinear eddies subsequently propagate westward and interact to form the striations (Qiu et al., 2013b). Fig. 13 shows the geographical distributions of L_{y3} for the most unstable short secondary waves along the ray path of the primary baroclinic Rossby waves. The black lines indicate the locations where the advection time scale of the primary baroclinic Rossby wave equals the e-folding time scale of the secondary waves. Fig. 13e shows the value of L_{y3} as a function of latitude, which reveals a clearer comparison that the meridionally-averaged L_{y3} values are 386, 393, 385, and 318 km based on the four situations in Fig. 13. The similar meridional wavelengths identified in Fig. 13a and b suggest that the semiannual period of the wind stress forcing hardly impacts the meridional scale of the breakdown baroclinic Rossby waves. Moreover, according to Fig. 13c, the baroclinic Rossby waves radiating from the non-meridional coastline ($\alpha = 45°$) also have no influence on the meridional length scale at their break down, when compared with Fig. 13b. Furthermore, Fig. 13d suggests that the reason for the smaller meridional scale (compared to Fig. 13b) is the shorter basin width.

5. Summary

Based on the Argo float trajectory data and gridded temperature/salinity data, we reconstructed the geostrophic currents in the NIO from the surface to 1200 db. The mid-depth eastward striations are located at 2° N, 6° N, 9.5° N, 12.5° N, 15.5° N, 17.5° N, 19.5° N, and 23° N in the Arabian Sea and their core depths appear above 500 db; however, in the Bay of Bengal, such striation-like structures are not clear. The meridional scale of the multiple zonal jets is ~400–600 km in the Pacific Ocean (Kessler and Gourdeau, 2006; Maximenko et al., 2008b) and ~300–500 km in the Atlantic Ocean (Table 3.1 in and Galperin and Read, 2019). Compared with the other ocean basins, the NIO striations typically have a smaller meridional scale of ~300 km. These observed features of the NIO striations based on the Argo observations are consistent with those simulated in the global eddy-resolving OFES model.

Limited by the no mean flow assumption and β-plane approximation, we used a nonlinear $1\frac{1}{2}$-layer reduced gravity model to explore the generation mechanism of the mid-depth striations in the open ocean in the NIO based on the triad baroclinic Rossby wave interaction theory. The mid-depth time-mean striations in the Arabian Sea are possibly generated by the nonlinear eddy interactions due to the breakdown of the wind-forced baroclinic Rossby waves. More specifically, the dominant semiannual wind variability over the NIO forces the eastward-propagating equatorial Kelvin waves. After impinging on the eastern

boundary, the equatorial Kelvin waves trigger the coastal trapped Kelvin waves and subsequently release a series of baroclinic Rossby waves from the eastern boundary. As the semiannual baroclinic Rossby waves propagate along their ray paths, they interact with the available secondary waves that can lead to triad instability. The primary baroclinic Rossby waves break down where the e-folding time scale of the most unstable secondary waves matches with the advective time scale of the primary waves, and this instability leads to the generation of isolated nonlinear eddies. The convergence of the potential vorticity fluxes associated with these eddies causes the formation of the striations.

The model results with semi-realistic coastlines reveal that the wind-forced equatorial Kelvin waves play the most crucial role in generating the alternating striations: while both the Arabian Sea and Bay of Bengal have a narrow basin scale, the width of the Arabian Sea (21°, averaged for the 6°–21° N band) is larger than the distance between the eastern boundary to the Rossby wave breakdown line (17°, averaged for the 6°–21° N band); however, the width of the Bay of Bengal (14°, averaged for the 6°–21° N band) is shorter than this distance. Thus, eddy-driven striations exist in the Arabian Sea, but are not observed in the Bay of Bengal. The striations appearing in the Arabian Sea are generated by the wind-forced equatorial Indian Ocean Kelvin waves that propagate into the NIO along the Bay of Bengal and the Indian subcontinent coastlines as coastal trapped Kelvin waves.

Thus, unlike the other studies that have considered the unstable boundary currents (Wang et al., 2012) or the fastest-growing instability pattern combined with the uniform background flow (Berloff et al., 2009b) to explain the generation of the alternating striations, we have used the triad Rossby wave interaction theory in the NIO. Our results have demonstrated that this theory is not only applicable to the North Pacific Ocean (Qiu et al., 2013b), but also to the NIO, and probably even to other ocean basins.

Acknowledgments

We thank Prof. Pavel Berloff and our anonymous reviewer for their constructive comments. The Argo data were collected and made freely available by the International Argo Program and the national programs that contribute to it. (http://www.argo.ucsd.edu, http://argo.jcommops.org). The Argo float trajectory data were acquired from the IFREMER (all trajectory data are available from ftp://ftp.ifremer.fr/ifremer/argo). The gridded T/S data were provided by Scripps Institution of Oceanography (http://sio-argo.ucsd.edu/RG_Climatology.html). The ANDRO Atlas was made by M. Ollitrault and J.-P. Ranou (doi:10.17882/47077). The OFES simulation was conducted on the Earth Simulator under the support of JAMSTEC (http://apdrc.soest.hawaii.edu/ESC/esgdata_main.php). This work is supported by the National Natural Science Foundation of China (41830538 and 41525019), the Chinese Academy of Sciences (XDA15020901, 133244KYSB20190031, ZDRW-XH-2019-2), the State Oceanic Administration of China (GASI-IPOVAI-02), the Southern Marine Science and Engineering Guangdong Laboratory (Guangzhou) (GML2019ZD0303, 2019BT2H594), and State Key Laboratory of Tropical Oceanography, (No. LTOZZ1802).

Appendix A. Supplementary data

Supplementary data related to this article can be found at https://doi.org/10.1016/j.dsr.2020.103307.

References

Ascani, F., Firing, E., Dutrieux, P., McCreary, J.P., Ishida, A., 2010. Deep equatorial ocean circulation induced by a forced-dissipated Yanai beam. J. Phys. Oceanogr. 40, 1118–1142. https://doi.org/10.1175/2010jpo4356.1.

Ascani, F., Firing, E., McCreary, J.P., Brandt, P., Greatbatch, R.J., 2015. The deep equatorial ocean circulation in wind-forced numerical solutions. J. Phys. Oceanogr. 45, 1709–1734. https://doi.org/10.1175/JPO-D14-0171.1.

Belmadani, A., Maximenko, N.A., McCreary, J.P., Furue, R., Melnichenko, O.V., Schneider, N., Di Lorenzo, E., 2013. Linear wind-forced beta plumes with application to the Hawaiian Lee Countercurrent. J. Phys. Oceanogr. 43, 2071–2094. https://doi.org/10.1175/JPO-D-12-0194.1, 10.1175/JPO-D-12-0194.1.

Berloff, P., Kamenkovich, I., Pedlosky, J., 2009a. A model of multiple zonal jets in the oceans: dynamical and kinematical analysis. J. Phys. Oceanogr. 39, 2711–2734. https://doi.org/10.1175/2009jpo4093.1.

Berloff, P., Kamenkovich, I., Pedlosky, J., 2009b. A mechanism of formation of multiple zonal jets in the oceans. J. Fluid Mech. 628, 395. https://doi.org/10.1017/S0022112009006375.

Berloff, P., Kamenkovich, I., 2013a. On spectral analysis of mesoscale eddies. Part I: linear analysis. J. Phys. Oceanogr. 43, 2505–2527. https://doi.org/10.1175/JPO-D-12-0232.1.

Berloff, P., Kamenkovich, I., 2013b. On spectral analysis of mesoscale eddies. Part II: nonlinear analysis. J. Phys. Oceanogr. 43, 2528–2544. https://doi.org/10.1175/JPO-D-12-0233.1.

Berloff, P., 2005. On rectification of randomly forced flows. J. Mar. Res. 63, 497–527. https://doi.org/10.1357/0022240054307894.

Chelton, D.B., DeSzoeke, R.A., Schlax, M.G., El Naggar, K., Siwertz, N., 1998. Geographical variability of the first baroclinic Rossby radius of deformation. J. Phys. Oceanogr. 28, 433–460. https://doi.org/10.1175/1520-0485(1998)028<0433:gvotfb>2.0.co;2.

Chen, C., Kamenkovich, I., Berloff, P., 2016. Eddy trains and striations in quasigeostrophic simulations and the ocean. J. Phys. Oceanogr. 46, 2807–2825. https://doi.org/10.1175/JPO-D-16-0066.1.

Cheng, X., Xie, S.-P., McCreary, J.P., Qi, Y., Du, Y., 2013. Intraseasonal variability of sea surface height in the Bay of Bengal. J. Geophys. Res. Oceans 118, 816–830. https://doi.org/10.1002/jgrc.20075.

Cravatte, S., Kessler, W.S., Marin, F., 2012. Intermediate zonal jets in the tropical Pacific Ocean observed by Argo floats. J. Phys. Oceanogr. 42, 1475–1485. https://doi.org/10.1175/jpo-d-11-0206.1.

Cravatte, S., Kestenare, E., Marin, F., Dutrieux, P., Firing, E., 2017. Subthermocline and intermediate zonal currents in the tropical Pacific Ocean: paths and vertical structure. J. Phys. Oceanogr. 47, 2305–2324. https://doi.org/10.1175/jpo-d-17-0043.1.

Davis, R.E., 2005. Intermediate-depth circulation of the Indian and South Pacific Oceans measured by autonomous floats. J. Phys. Oceanogr. 35, 683–707. https://doi.org/10.1175/jpo2702.1.

Galperin, B., Nakano, H., Huang, H.P., Sukoriansky, S., 2004. The ubiquitous zonal jets in the atmospheres of giant planets and Earth's oceans. Geophys. Res. Lett. 31 https://doi.org/10.1029/2004gl019691.

Galperin, B., Read, P.L., 2019. Zonal Jets Phenomenology, Genesis, and Physics. Cambridge University Press, p. 46.

Kessler, W.S., Gourdeau, L., 2006. Wind-driven zonal jets in the south Pacific Ocean. Geophys. Res. Lett. 33, L03608. https://doi.org/10.1029/2005GL025084.

Khatri, H., Berloff, P., 2019. Tilted drifting jets over a zonally sloped topography: effects of vanishing eddy viscosity. J. Fluid Mech. 876, 939–961. https://doi.org/10.1017/jfm.2019.579.

Lebedev, K.V., Yoshinari, H., Maximenko, N.A., Hacker, P.W., 2007. YoMaHa'07: velocity data assessed from trajectories of Argo floats at parking level and at the sea surface. IPRC Tech. Note 4, 16.

Maximenko, N.A., Bang, B., Sasaki, H., 2005. Observational evidence of alternating zonal jets in the world ocean. Geophys. Res. Lett. 32 https://doi.org/10.1029/2005gl022728.

Maximenko, N.A., Melnichenko, O.V., Niiler, P.P., Sasaki, H., 2008. Stationary mesoscale jet-like features in the ocean. Geophys. Res. Lett. 35 (8), L08603. https://doi.org/10.1029/2008gl033267.

Nakano, H., Hasumi, H., 2005. A series of zonal jets embedded in the broad zonal flows in the pacific obtained in eddy-permitting ocean general circulation models. J. Phys. Oceanogr. 35, 474–488. https://doi.org/10.1175/jpo2698.1.

Ogata, T., Xie, S.-P., 2011. Semiannual cycle in zonal wind over the equatorial Indian Ocean. J. Clim. 24, 6471–6485. https://doi.org/10.1175/2011JCLI4243.1.

Ollitrault, M., Rannou, J.-P., 2013. ANDRO: an argo-based deep displacement dataset. J. Atoms. Oceanic Technol. 30, 759–788. https://doi.org/10.1175/jtech-d-12-00073.1.

Ollitrault, M., de Verdiere, A.C., 2014. the ocean general circulation near 1000-m depth. J. Phys. Oceanogr. 44, 384–409. https://doi.org/10.1175/jpo-d-13-030.1.

Park, J.J., Kim, K., Crawford, W.R., 2004. Inertial currents estimated from surface trajectories of ARGO floats. Geophys. Res. Lett. 31 https://doi.org/10.1029/2004gl020191.

Park, J.J., Kim, K., King, B.A., Riser, S.C., 2005. An advanced method to estimate deep currents from profiling floats. J. Atoms. Oceanic Technol. 22, 1294–1304. https://doi.org/10.1175/jtech1748.1.

Park, J.J., Kim, K., 2013. Deep currents obtained from Argo float trajectories in the Japan/East Sea. Deep-Sea Res. PT II 85, 169–181. https://doi.org/10.1016/j.dsr2.2012.07.032.

Pedlosky, J., 1987. Geophysical Fluid Dynamics. Springer-Verlag, p. 710.

Picaut, J., Tournier, R., 1991. Monitoring the 1979-1985 equatorial pacific current transports with expendable bathythermograph data. J. Geophys. Res. Oceans 96. https://doi.org/10.1029/90JC02066.

Qiu, B., Rudnick, D.L., Chen, S., Kashino, Y., 2013a. Quasi-stationary North Equatorial undercurrent jets across the tropical North Pacific ocean. Geophys. Res. Lett. 40, 2183–2187. https://doi.org/10.1002/grl.50394.

Qiu, B., Chen, S., Sasaki, H., 2013b. Generation of the north equatorial undercurrent jets by triad baroclinic Rossby wave interactions. J. Phys. Oceanogr. 43, 2682–2698. https://doi.org/10.1175/jpo-d-13-099.1.

Qiu, B., Chen, S., Hacker, P., Hogg, N., Jayne, S., Sasaki, H., 2008. The Kuroshio Extension northern recirculation gyre: profiling float measurements and forcing mechanism. J. Phys. Oceanogr. 38, 1764–1779. https://doi.org/10.1175/2008JPO3921.1.

Rhines, P.B., 1975. Waves and turbulence on A beta-plane. J. Fluid Mech. 69, 417–443. https://doi.org/10.1017/s0022112075001504.

Rhines, P.B., Holland, W.R., 1979. A theoretical discussion of eddy driven mean flows. Dynam. Atmos. Oceans 3, 289–325. https://doi.org/10.1016/0377-0265(79)90015-0.

Richards, K.J., Maximenko, N.A., Bryan, F.O., Sasaki, H., 2006. Zonal jets in the Pacific Ocean. Geophys. Res. Lett. 33 https://doi.org/10.1029/2005gl024645.

Roemmich, D., D, Gilson, J., 2009. The 2004–2008 mean and annual cycle of temperature, salinity, and steric height in the global ocean from the Argo program. Prog. Oceanogr. 82, 81–100. https://doi.org/10.1016/j.pocean.2009.03.004.

Sasaki, H., Nonaka, M., Masumoto, Y., Sasai, Y., Uehara, H., Sakuma, H., 2008. An eddy-resolving hindcast simulation of the quasiglobal ocean from 1950 to 2003 on the Earth simulator. In: Ohfuchi, W., Hamilton, K. (Eds.), High Resolution Numerical Modelling of the Atmosphere and Ocean. Springer, pp. 157–186.

Schopf, P.S., Anderson, D.L.T., Smith, R., 1981. Beta-dispersion of low-frequency Rossby waves. Dynam. Atmos. Oceans 5, 187–214. https://doi.org/10.1016/0377-0265(81)90011-7.

Schott, F.A., Xie, S.-P., McCreary Jr., J.P., 2009. Indian ocean circulation and climate variability. Rev. Geophys. 47 https://doi.org/10.1029/2007rg000245.

van Sebille, E.V., Kamenkovich, I., Willis, J.K., 2011. Quasi-zonal jets in 3-D Argo data of the northeast Atlantic *Geophys*. Res. Lett. 38.

Wang, J., Spall, M.A., Flierl, G.R., Malanotte-Rizzoli, P., 2012. A new mechanism for the generation of quasi-zonal jets in the ocean. Geophys. Res. Lett. 39 https://doi.org/10.1029/2012gl051861.

Xie, J., Zhu, J., 2008. Estimation of the surface and mid-depth currents from Argo floats in the Pacific and error analysis. J. Mar. Syst. 73, 61–75. https://doi.org/10.1016/j.jmarsys.2007.09.001.